

The peculiar disk evolution of 4U 1630–472 observed by Insight-HXMT during the 2022 and 2023 outbursts

JING-QIANG PENG^{*} ^{1,2} SHU ZHANG^{*} ¹ QING-CANG SHUI^{*} ^{1,2} YU-PENG CHEN ¹ SHUANG-NAN ZHANG ^{1,2}
LING-DA KONG ³ A. SANTANGELO³ ZHUO-LI YU¹ LONG JI ⁴ PENG-JU WANG ³ ZHI CHANG ¹ JIAN LI^{5,6} AND
ZHAO-SHENG LI ⁷

¹Key Laboratory of Particle Astrophysics, Institute of High Energy Physics, Chinese Academy of Sciences, 100049, Beijing, China

²University of Chinese Academy of Sciences, Chinese Academy of Sciences, 100049, Beijing, China

³Institute für Astronomie und Astrophysik, Kepler Center for Astro and Particle Physics, Eberhard Karls, Universität, Sand 1, D-72076 Tübingen, Germany

⁴School of Physics and Astronomy, Sun Yat-Sen University, Zhuhai, 519082, China

⁵CAS Key Laboratory for Research in Galaxies and Cosmology, Department of Astronomy, University of Science and Technology of China, Hefei 230026, China

⁶School of Astronomy and Space Science, University of Science and Technology of China, Hefei 230026, China

⁷Key Laboratory of Stars and Interstellar Medium, Xiangtan University, Xiangtan 411105, Hunan, China

ABSTRACT

We study the spectral properties of the black hole X-ray transient binary 4U 1630–472 during the 2022 and 2023 outbursts with Insight-HXMT observations. We find that the outbursts are in peculiar soft states. The effect of the hardening factor on the disk temperature is taken into account by $kerrbb$, and the flux and temperature of the disk are found to follow $F \propto T_{\text{eff}}^{3.92 \pm 0.13}$ and $F \propto T_{\text{eff}}^{4.91 \pm 1.00}$, for the two outbursts respectively. The flux-temperature relation is roughly consistent with holding a standard disk. By fitting with the p-free model, the p-value is found to have anti-correlation with disk temperature. Combined a joint diagnostic in a diagram of the relation between the non-thermal fraction and luminosity, by enclosing as well the previous outbursts, reveals a possible pattern for the disk evolution toward a slim one, and such an evolution may depend on the fraction of the non-thermal emission in the high soft state.

Keywords: X-rays: binaries — X-rays: individual (4U 1630–472)

1. INTRODUCTION

Black hole X-ray binaries (BHXRBs) can be classified as persistent or transient sources. For transient sources, both the accretion rate and the disk temperature are relatively low during long periods in the quiescent state (Deegan et al. 2009; Tetarenko et al. 2016a). When the temperature of the disk increases, neutral hydrogen within the outer part of the disk becomes ionized, triggering thermal and viscous instabilities. Consequently, the black hole X-ray binary undergoes an outburst, ac-

companied by the increase of X-ray emission (Cannizzo et al. 1995; Lasota 2001; Belloni et al. 2011).

The outbursts of black hole X-ray binaries usually go through different spectral states. Different spectral states will have different spectral and timing characteristics. For the Low/Hard states (LHS), the emission is dominated by non-thermal emission. Occasionally, it will be accompanied by low-frequency quasi-periodic oscillations (LFQPOs), mainly C-type. The High/Soft state (HSS) emission is dominated by thermal radiation from the disk, characterized additionally by weak noise components in the power density spectrum (PDS). As the accretion rate rises, the black hole X-ray binary may enter the very high state (VHS) (also called the steep power-law (SPL) state), during which the spectral index Γ is greater than 2.4 and sometimes QPOs of 0.1–30

pengjq@ihep.ac.cn

szhang@ihep.ac.cn

shuiqc@ihep.ac.cn

Hz appear in the PDS (Thorne & Price 1975; Tanaka & Shibazaki 1996; Belloni et al. 2005).

Black hole X-ray binary outbursts are highly driven by the evolution of the accretion disk. Accretion models in black hole X-ray binaries evolved into the Shakura-Sunyaev Disk (SSD), Shapiro-Lightman-Eardley (SLE) disk, slim disk, and advection-dominated accretion flow (ADAF). SSDs are geometrically thin, optically thick, and referred to as the standard disk. The structure and radiation of the stabilized accretion disk can be determined by three fundamental parameters: the coefficient of viscosity α , the mass of the central star M , and the accretion rate \dot{M} . For the BHXRBs, the accretion disk is likely truncated at the inner part at a distance far from black hole and is usually considered as a standard one in the soft state (Shakura & Sunyaev 1973). SLE disks are governed by gas pressure and characterized by different temperatures of the ion and electron populations. SLE disks can generate intense X-ray and gamma-ray radiation but are thermally unstable (Shapiro et al. 1976; Piran 1978). ADAFs are geometrically thick and optically thin and dominated by gas pressure. They can maintain viscosity and thermal stability (Narayan & Yi 1995; Abramowicz et al. 1995), and hence are commonly utilized in modeling the non-thermal emission of the outbursts (Esin et al. 1997; Kylafis & Belloni 2015). Although ADAFs have low radiation efficiency, the high-temperature electrons within them can scatter soft photons from SSDs through the inverse Compton procedure, producing a significant amount of non-thermal emission. Slim disks, also known as optically thick ADAFs, were introduced to be optically and geometrically thick by Abramowicz et al. (1988), with radiation efficiency lower than the standard disk and the disk emission following $L_{\text{disk}} \propto T_{\text{in}}^2$.

4U 1630–472 is a transient low-mass black hole X-ray binary system that was first discovered by the Uhuru satellite in 1969 (Giacconi et al. 1972). This system is well known for its X-ray outburst repeating period of 600–650 days (Jones et al. 1976; Kuulkers et al. 1997; Tetarenko et al. 2016b). A high hydrogen absorption column density was observed as $N_{\text{H}} = (4 - 12) \times 10^{22} \text{ cm}^{-2}$ (Tomsick et al. 1998). One of the peculiar behaviors for 4U 1630–472 is that the low hard state was hardly caught in the initial outburst phase (Abe et al. 2005; Tomsick et al. 2014), similar to outbursts observed in other sources such as MAXI J0637–430 and SLX 1746–331 (Ma et al. 2022; Peng et al. 2023, 2024). 4U 1630–472 was observed to have a black hole mass of about $10 M_{\odot}$ (Seifina et al. 2014), an inclination of 65° (Kuulkers et al. 1998), and a distance between 4.7 and 11.5 kpc (Kalemci et al. 2018).

For the black hole spin, Liu et al. (2022) reported $a = 0.817 \pm 0.014$ using Insight-HXMT data, and King et al. (2014) obtained $0.985_{-0.014}^{+0.005}$ by fitting the spectrum of NuSTAR. Abe et al. (2005) classified the disk of 4U 1630–472 into three states with a series of outbursts observed in 1996–2006 by RXTE. IXPE observation of 4U 1630–472 in HSS of the 2022 outburst revealed very high polarization (from $\sim 6\%$ at 2 keV to $\sim 10\%$ at 8 keV), which is not consistent with the standard thin accretion disk model (Ratheesh et al. 2024). Ratheesh et al. (2024) suggested that matter is accreted onto the black hole through a thin disk covered with a partially ionized atmosphere that flows away at mildly relativistic speeds.

In this paper, we perform a detailed spectral analysis by taking Insight-HXMT observations. We report the evolution of the disk during the 2022 and 2023 outbursts. Section 2 describes the observations and data reduction. The detailed results are presented in Section 3. The results are then discussed and concluded in Section 4.

2. OBSERVATIONS AND DATA REDUCTION

2.1. *Insight-HXMT*

Insight-HXMT is the first Chinese X-ray astronomy satellite, successfully launched on 2017, June 15 (Zhang et al. 2014, 2018, 2020). It carries three scientific payloads: the low energy X-ray telescope (LE, SCD detector, 1–15 keV, 384 cm^2 , Chen et al. 2020), the medium energy X-ray telescope (ME, Si-PIN detector, 5–35 keV, 952 cm^2 , Cao et al. 2020), and the high energy X-ray telescope (HE, phoswich NaI (CsI), 20–250 keV, 5100 cm^2 , Liu et al. 2020).

Insight-HXMT observed 4U 1630–472 from August 6, 2022 (MJD 59797) to May 3, 2023 (MJD 60070). We extract the data from LE, ME and HE using the Insight-HXMT Data Analysis software HXMTDAS v2.06. The data are filtered with the criteria recommended by the Insight-HXMT Data Reduction Guide v2.06¹. Due to the large detector noise peaks in the low-energy region of the LE, the energy bands considered for spectral analysis and light curves are LE 2–8 keV, ME 8–28 keV and HE 28–100 keV. One percent systematic error is added to data (Liao et al. 2020), and errors are estimated via Markov Chain Monte-Carlo (MCMC) chains with a length of 20000.

3. RESULTS

3.1. *Light curve and Hardness-intensity diagram*

¹ <http://hxmtweb.ihep.ac.cn/SoftDoc/648.jhtml>

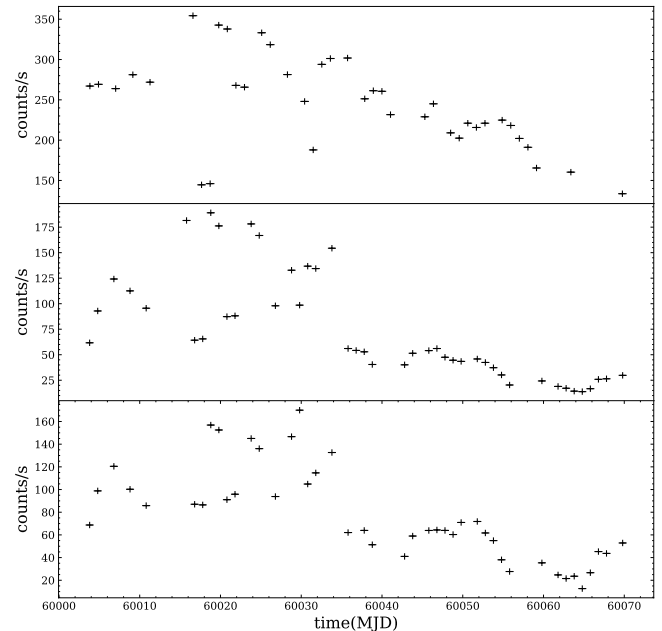
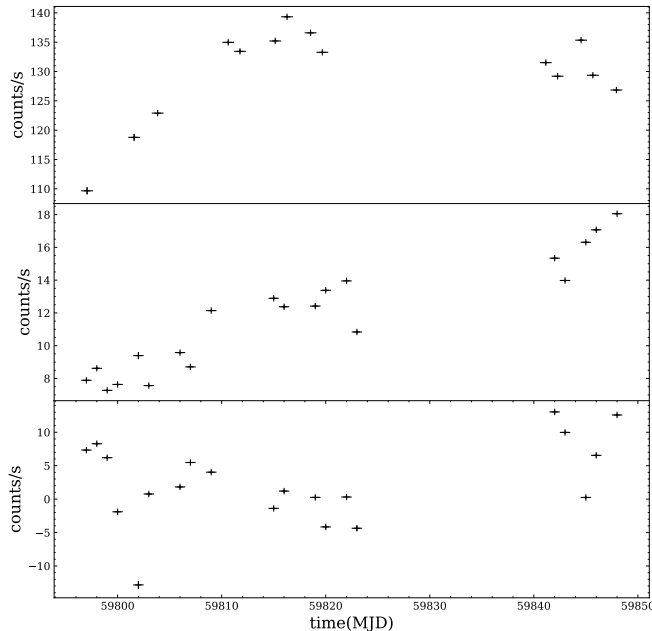


Figure 1. The light curves of 4U 1630–472 observed by Insight-HXMT during 2022 and 2023 outbursts. Top panel: the light curve of Insight-HXMT LE in 2–8 keV. Middle panel: the light curve of Insight-HXMT ME in 10–28 keV. Bottom panel: the light curve of Insight-HXMT HE in 28–100 keV.

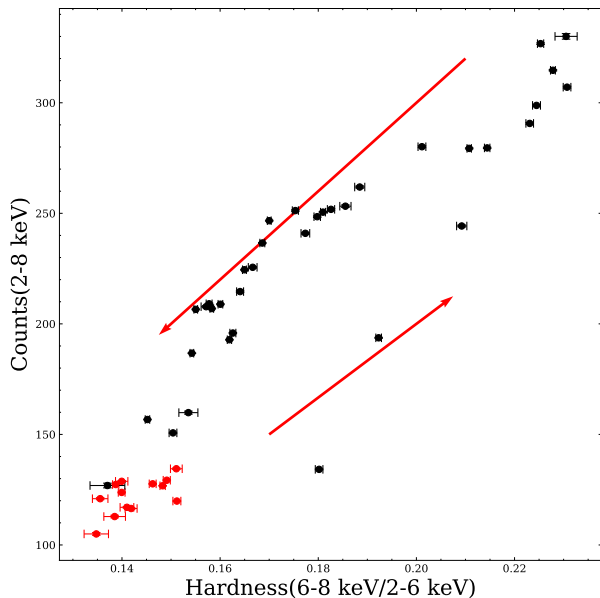


Figure 2. The hardness-intensity diagram of 4U 1630–472, where the hardness is defined as the ratio of 6–8 keV to 2–6 keV count rate. The black and red dots represent the 2022 and 2023 outbursts of 4U 1630–472 observed by Insight-HXMT.

Figure 1 shows the light curve of Insight-HXMT observations of 4U 1630–472, where two outbursts stand out in 2022 and 2023, respectively.

We extract the 2–6 keV, 6–8 keV, and 2–8 keV light curves of Insight-HXMT to construct the Hardness-Intensity Diagram (HID) of 4U 1630–472. The hardness

is defined as the count rate ratio of 6–8 keV to 2–6 keV, while the intensity takes the count rate of 2–8 keV. As shown in Figure 2, the HID from Insight-HXMT observations suggests that the source evolved from 2022 to 2023 with a harder spectrum.

3.2. The spectral analysis

3.2.1. *diskbb*

The spectral fitting is carried out using the software package XSPEC V12.13.1. We adopt several models to fit the spectrum of Insight-HXMT. The `tbabs` is taken to account for interstellar absorption (Wilms et al. 2000), with photoelectric cross-sections provided by Verner et al. (1996), and the disk component is fitted with `diskbb` (Mitsuda et al. 1984). To consider the differences in the effective area of the calibration between different instruments (Chen et al. 2018). `constant` is introduced to balance the calibration discrepancies of Insight-HXMT LE, ME, and HE (in this paper, we fix the constant of LE to 1). At this time, we find that the fit is not good ($\chi^2/(\text{d.o.f})=2067.17/897=3.25$) and the residual showing up in the middle energies stimulates us to improve the fit by convolving with an additional component of `thcomp`. Finally, the fit is largely improved $\chi^2/(\text{d.o.f})=879.29/895=0.98$ (see Figure 5). Therefore our fitting model M1 is: `constant*tbabs*thcomp*diskbb`. The flux of the disk in the 1–100 keV is estimated with `cflux`. we first act `cflux` on `diskbb` to compute the thermal flux. Then act on the `comp` to get the total flux (thermal plus non-

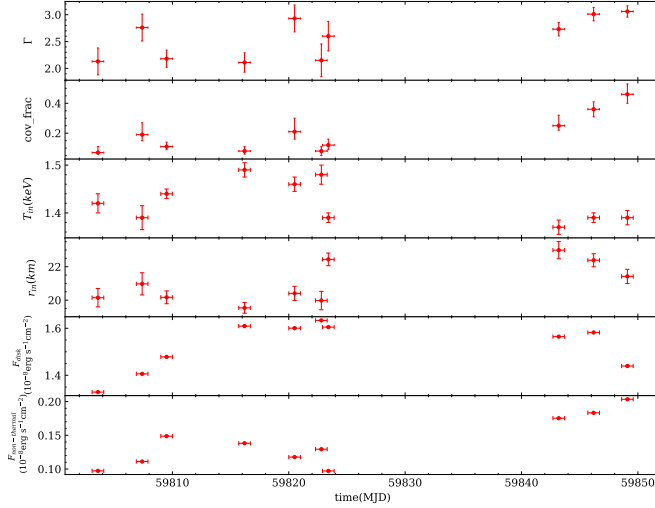


Figure 3. Evolution of the spectral parameters of 4U 1630–472 in 2022 and 2023 from model M1: Γ is the low-energy power-law photon index, T_{in} the temperature of the inner disk, Cov_frac the coverage factor, and r_{in} the inner radius of the disk. F_{disk} and $F_{\text{non-thermal}}$ are disk flux and non-thermal flux, respectively. The red dots represent data points with relatively low fluxes, including the 2022 outburst and three low-flux data in the 2023 outburst, while the black dots correspond to high flux data for 2023.

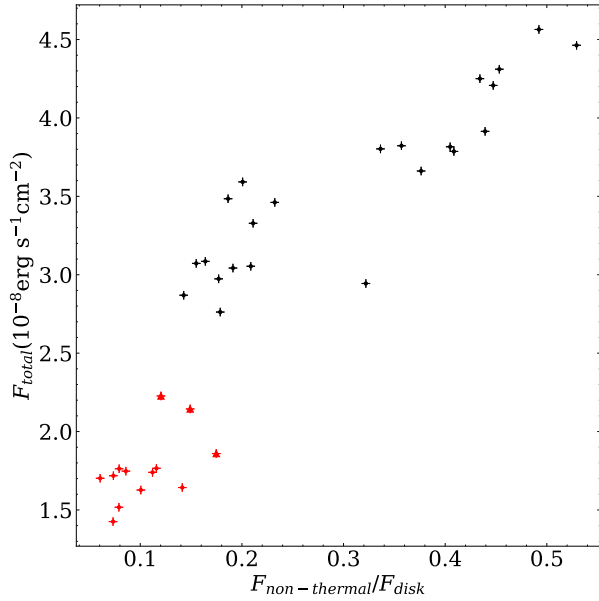


Figure 4. The hardness-intensity diagram of 4U 1630–472, where the hardness is defined as the ratio of F_{disk} to $F_{\text{non-thermal}}$. The colors inherit those in Figure 3. The three data with the lowest flux in the 2023 outburst are plotted with triangles.

thermal flux) then subtract the thermal flux to get the non-thermal flux.

The parameters obtained from spectral fitting with M1 are shown in Table 1 of the appendix A. The evolutions of the spectral parameters are shown in Figure 3. The three data points in the ending phase of the 2023 outburst exhibited lower fluxes, leading us to group them with the 2022 outburst data (represented by the

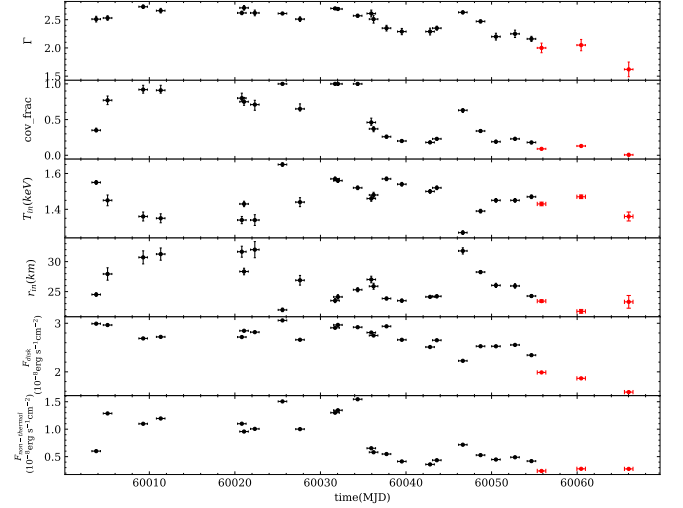


Figure 5. Spectral fit of M1 for 4U 1630–472 of Obs P040426302301. The black, red, and green symbols correspond to the LE, ME, and HE data from Insight-HXMT, respectively.

red points in Figure 3). As shown in Figure 4, from the HID with the hardness ratio defined as the ratio of the non-thermal flux to the disk flux, it seems that these three data points (plotted in triangles in Figure 4) are more aligned with the 2022 outburst in terms of their position on the HID. We conduct a KS-test on the red and black data in Figure 3 and find that their p-values are 0.0002, indicating that they are not suggestive of the same distribution. We also conducted a KS-test on the last three red data and the data from the 2022 outburst, with a p-value of 0.14, indicating that they are likely suggestive of the same distribution. We free the column

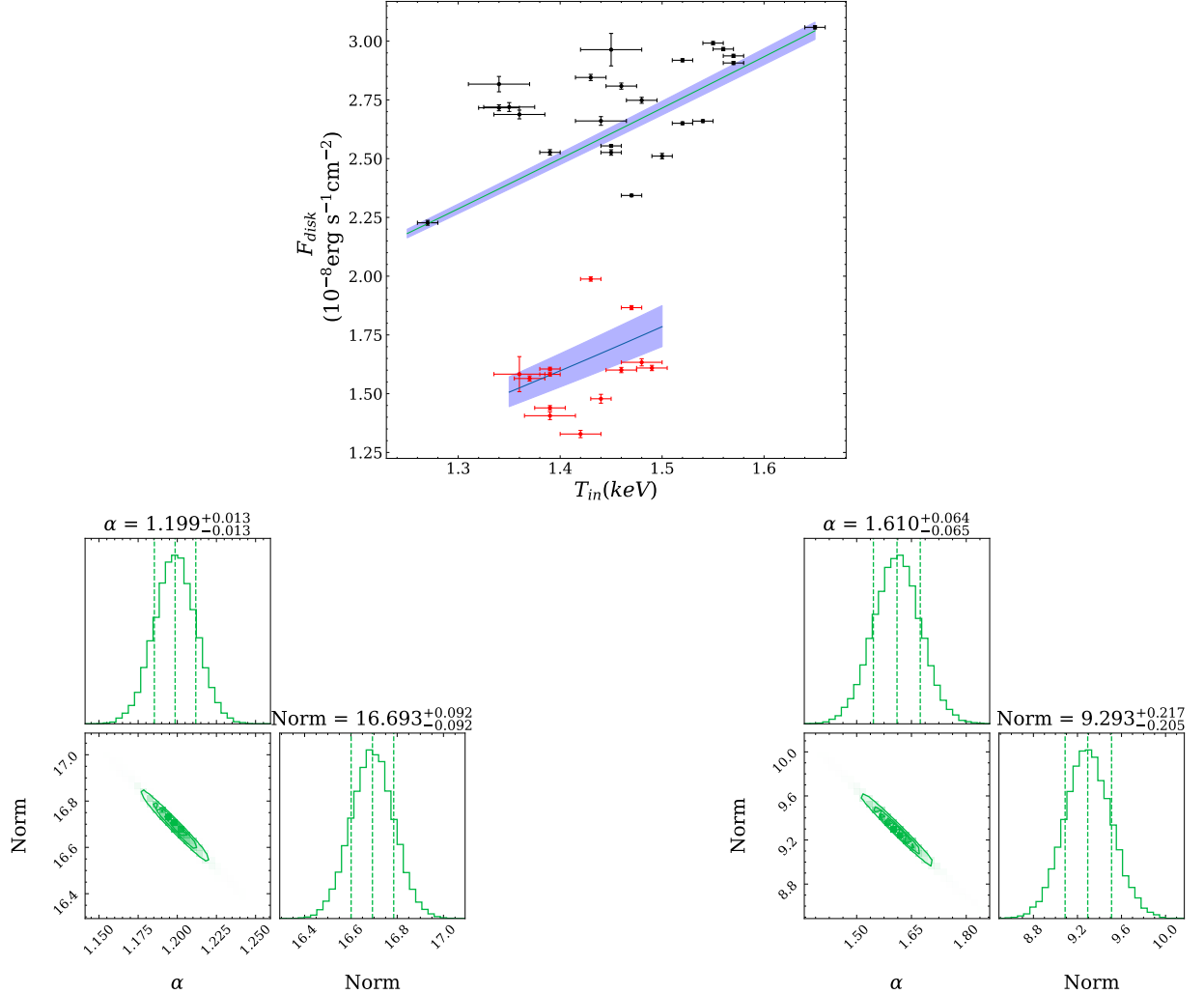


Figure 6. The relationship between inner disk temperature and flux. Red and black points inherit the colors illustrated in Figure 3. The green and blue lines represent the relationship of $F_{\text{disk}} \propto T_{\text{in}}^{\alpha}$, where $\alpha_1 = 1.20 \pm 0.01$ and $\alpha_2 = 1.61 \pm 0.06$. The two subfigures below are One- and two-dimensional projections of the posterior probability distributions, and the 0.16, 0.5 and 0.84 quantile contours derived from the MCMC analysis for two parameters.

density N_H during the fitting of the outburst in 2022 and 2023 and get values around $6.5 \times 10^{22} \text{ cm}^{-2}$, and thus we fix it at $6.5 \times 10^{22} \text{ cm}^{-2}$ thereafter. The inner disk radius r_{in} can be estimated from the normalization of the disk obtained from M1: $\text{norm} = \left(\frac{r_{\text{in}}}{D_{10}}\right)^2 \cos \theta$, where r_{in} is the inner disk radius, D_{10} is the distance of the source in units of 10 kpc (10 kpc), and θ is the inclination angle (65°).

As shown in Figure 6, We employ the Markov Chain Monte Carlo (MCMC) method with the Goodman-Weare algorithm employing 8 walkers and a total chain length of 40,000 iterations (Goodman & Weare 2010). The initial 2000 elements of the chain were discarded as a "burn-in" period to ensure convergence and stability of the fit. The distributions of the inner disk temperature (T_{in}) and the flux of the disk (F_{disk}) are

diffuse and power-law fits give $F_{\text{disk}} \propto T_{\text{in}}^{1.20 \pm 0.01}$ and $F_{\text{disk}} \propto T_{\text{in}}^{1.61 \pm 0.06}$, which are largely deviating from T_{in}^4 expected for a standard disk. Such deviation could potentially be attributed to the variable hardening factor. Consequently, our measured r_{in} and T_{in} may not represent the intrinsic ones.

3.2.2. *kerrbb*

To investigate the effect of the hardening factor on measurements of the temperature and the inner radius of the disk, we replace *diskbb* with *kerrbb* thus have the have model M2: `constant*tbabs*thcomp*kerrbb`. With eta, mass, spin, inclination, and distance fixed at 0, $10 M_{\odot}$, 0.9, 65° , and 10 kpc, respectively (Kuulkers et al. 1998; Seifina et al. 2014; Kalemci et al. 2018), and normalization at 1 as required by the model, fit with model M2 results in $\chi^2/(\text{d.o.f.})=1.15$ (see Figure 8).

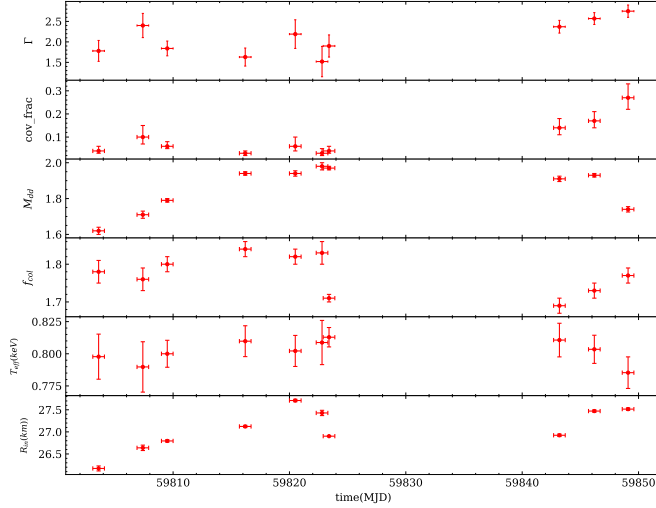


Figure 7. Evolution of the spectral parameters of 4U 1630–472 in 2022 and 2023 from model M2: Γ is the low-energy power-law photon index, Cov_frac the coverage factor, M_{dd} the “effective” mass accretion rate of the disk in units of 10^{18} g/s, f_{col} the spectral hardening factor and T_{eff} the effective temperature of the inner zone of the disk, obtained by T_{in}/f_{col} , and R_{in} the inner radius of the disk. The colors inherit those in Figure 3.

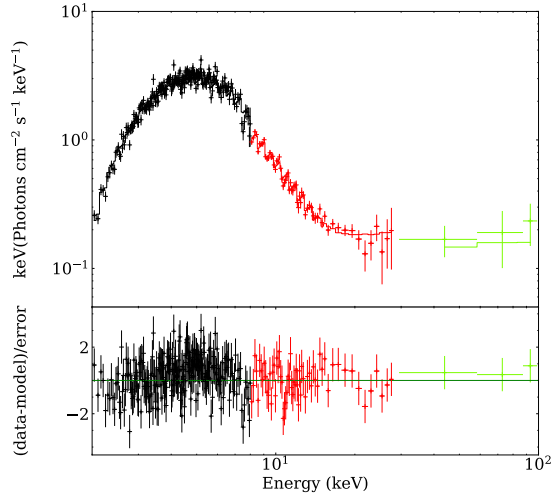


Figure 8. Spectral fit of M2 for 4U 1630–472 of Obs P040426302301. The black, red, and green symbols correspond to the LE, ME, and HE data from Insight-HXMT, respectively.

The spectral parameters born out of M2 are shown in Figure 7 and Table 2 of the appendix A., where R_{in} is calculated with $R_{in} = f_{col}^2 \xi r_{in}$ (Makishima et al. 2000), here, f_{col} is a spectral hardening factor (Shimura & Takahara 1995a), and ξ is set to 0.41 (Kubota et al. 1998) to correct the inner boundary condition. The effective temperature (T_{eff}) is determined by T_{in} with the hardening factor. After introducing the hardening factor, the inner radius R_{in} becomes relatively stable, and the temperature dependence of the disk flux turns out to be $T_{eff}^{3.92 \pm 0.13}$ and $T_{eff}^{4.91 \pm 1.00}$ for the 2022 and 2023 outbursts, respectively, with the same fitting method as in

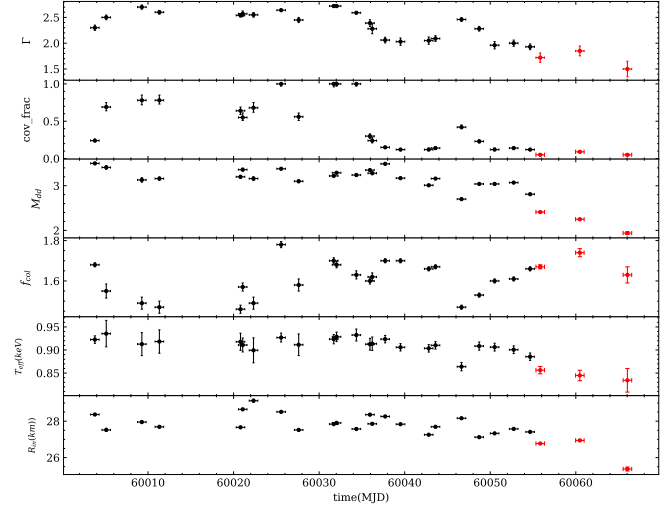


Figure 6 (Figure 9). However, it is noticeable that the uncertainties in the power law indices obtained from the fitting are relatively large. Figure 10 shows the flux dependence of the hardening factor derived from the 2022 and 2023 outbursts. The pink stars are the mean value calculated by dividing the four data into one group. We find that the hardening factor decreases with increasing luminosity, but the distribution is more diffuse at high luminosity. The Spearman rank-order correlation coefficient and p-value were obtained by the Spearman rank-order test as -0.73 and 0.024 respectively, briefly consistent with the theoretical evolution trend from Merloni et al. (2000); Ren et al. (2022). Given the flux-dependence of the hardening factor and the rough consistency with T_{in}^4 of the disk flux, 2022 and 2023 outbursts may still hold a standard disk.

3.2.3. *diskpbb*

To further investigate the possible deviation of 4U 1630–472 disks from a standard disk, we replace *diskbb* with *diskpbb*. Therefore, our model 3 is represented as `constant*tbabs*(thcomp*diskpbb)`, and the fit results in $\chi^2/(d.o.f.)=0.97$ (see Figure 12). *Diskpbb* is a multiple blackbody disk model with local disk temperature $T(r)$ proportional to r^{-p} , where p is a free parameter. p takes 0.75 for the standard disk and 0.5 for the slim disk. (Mineshige et al. 1994; Hirano et al. 1995; Watarai et al. 2000a; Kubota & Makishima 2004). The average of p is $0.81^{+0.13}_{-0.12}$ for the 2022 outburst and $0.67^{+0.09}_{-0.07}$ for the 2023 outburst (Figure 11). For both outbursts, a standard disk can not be excluded due to that 0.75 is covered by the averaged p within 1σ error bars, but a slim disk is not likely supported since 0.5 is

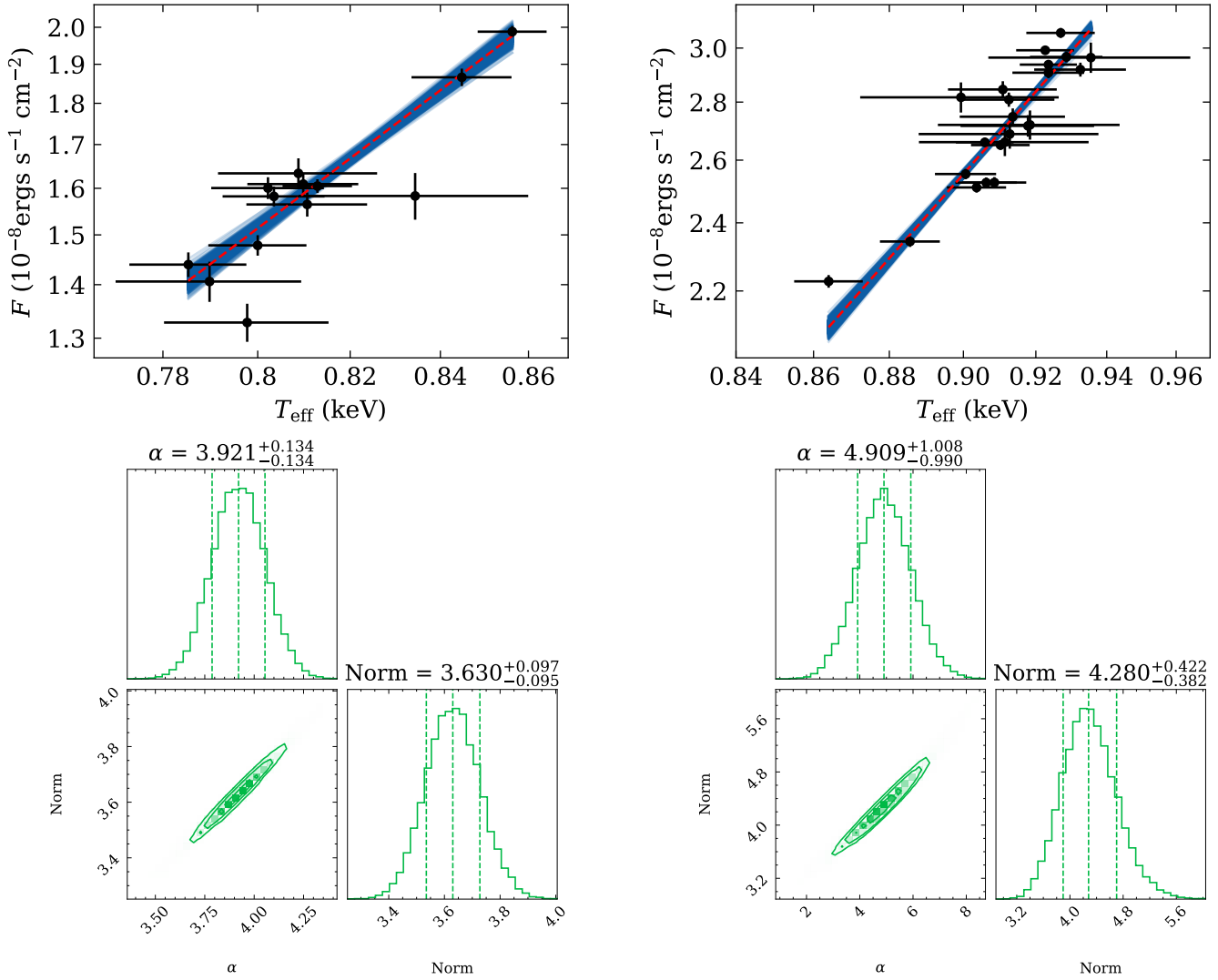


Figure 9. The disk unabsorbed flux (1–100 keV) versus the disk inner temperature (T_{eff}). Flux correlates with temperature in forms of $T_{\text{eff}}^{3.92 \pm 0.13}$ and $T_{\text{eff}}^{4.91 \pm 1.00}$ during the 2022 (left) and 2023 (right) outbursts, respectively. The two subfigures below are One- and two-dimensional projections of the posterior probability distributions, and the 0.16, 0.5 and 0.84 quantile contours derived from the MCMC analysis for two parameters.

not covered by the averaged p even within 2σ of the errorbars. The parameters obtained from spectral fitting with M3 are shown in Table 3 of the appendix A. The evolution of p with T_{in} as shown in Figure 13, indicates that p of the 2022 outburst is generally larger than that of the 2023 outburst. We use the linregress function to fit the temperature and p . Linear fits result in slopes of -1.53 and -0.22 for the 2022 and 2023 outbursts. The reduced chi-square and degrees of freedom are 2.71, 11 and 4.33, 21, respectively. We also test their correlation using Spearman rank-order and obtain correlation coefficients and p-values of -0.86 , 0.0002 and -0.56 , 0.005 respectively. It turns out that, for outbursts from 2022 to 2023, p decreases monotonously with temperature and

thus suggests a disk may continuously evolve toward a slim one with decreasing radiative efficiency.

4. DISCUSSION AND CONCLUSION

We have conducted spectral analyses of the outbursts of 4U 1630–472 observed by Insight-HXMT in 2022 and 2023. We find that during the 2022 and 2023 outbursts, the distributions of the inner disk temperature against the flux are scattered around $F_{\text{disk}} \propto T_{\text{in}}^{1.2}$ and $F_{\text{disk}} \propto T_{\text{in}}^{1.6}$, which are not consistent with the standard disk hypothesis. By considering additionally the hardening factor, these relations move to $F \propto T_{\text{eff}}^{3.92 \pm 0.13}$ and $F \propto T_{\text{eff}}^{4.91 \pm 1.00}$. With a p -free model, although the standard disk can not be excluded, an evolution of decreasing p with disk temperature is visible.

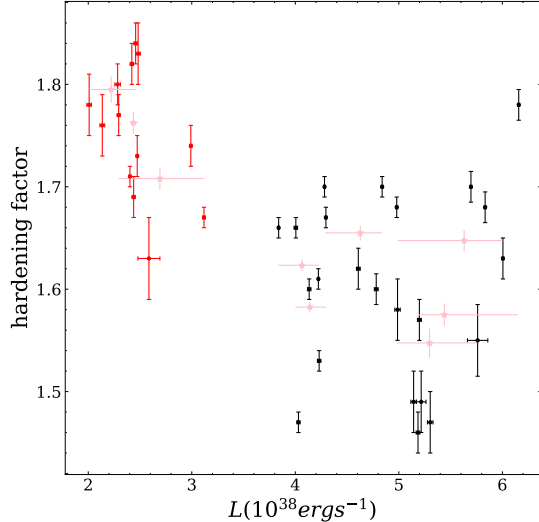


Figure 10. Evolution of hardening factor with luminosity. The pink stars are the mean values calculated by combining the neighboring four data.

Abe et al. (2005) classified the soft state of 4U 1630–472 into three states with RXTE observations of five outbursts spanning from 1996 to 2004. In the first state, the disk behaves like a standard one. The accretion disk model can well explain the X-ray spectrum of this state, the disk temperature $T_{\text{in}} < 1.2\text{keV}$, and the X-ray luminosity is less than $2.5 \times 10^{38}\text{erg/s}$. The disk flux follows the $L_{\text{disk}} \propto T_{\text{in}}^4$, indicating that the accretion disk structure is consistent with the standard thin disk model. In the second state, the spectrum appears similar to the standard state, but the relationship between disk flux and temperature is $L_{\text{disk}} \propto T_{\text{in}}^2$, indicating that the accretion disk radiation efficiency is relatively low. An optically thick, convection-dominated “slim disk” may have formed. In the third state, the accretion disk temperature and luminosity are similar to the standard state, but there is a strong high-energy Comptonized component. This may be due to the inverse Compton scattering process converting part of the disk radiation into a high-energy component. Accordingly, they defined three regimes in the hard emission fraction-total luminosity diagram: standard, apparently standard, and anomalous regimes. The outbursts in 2022 and 2023 as observed by Insight-HXMT contribute two more samples for investigating the evolution of the accretion disk between different regimes.

For the 2022 and 2023 outbursts, model M1 gives the disk flux-temperature relations not following $F \propto T_{\text{in}}^4$. Scattering by the accretion disk atmosphere can lead to disk emission deviating from a standard correlation with the temperature (Madej 1974). Shimura & Takahara (1995b) demonstrated that such a deviation can

be largely alleviated by introducing a hardening factor. After considering the impact of the hardening factor on the temperature and radius of the disk, the flux and temperature of the disk can be presented in functions of $F \propto T_{\text{eff}}^{3.92 \pm 0.13}$ and $F \propto T_{\text{eff}}^{4.91 \pm 1.00}$, suggesting a standard disk may still hold in the 2022 and 2023 outbursts. Ratheesh et al. (2024) analyzed the 2022 IXPE observations of 4U 1630–472 and concluded that the observed polarization properties are compatible with the accretion of matter onto the black hole at a mildly relativistic rate through a thin disk covered by a partially ionized atmosphere. The apparent deviation for the relation of disk flux and temperature from standard disk and the introduction of the hardening factor in outbursts of 2022 and 2023 are in line with the picture proposed with IXPE observations.

The further investigation of the disk properties with a p-free model gives averaged p of $0.81^{+0.13}_{-0.12}$ for the 2022 outburst and $0.67^{+0.09}_{-0.07}$ for 2023 outburst. Again, both cover 0.75 for a standard disk but away from 0.5 for a slim disk (Watarai et al. 2000b). Albeit all the aforementioned disk features for the two outbursts can be roughly in line with a standard one, p is found to evolve significantly along with the outbursts. As shown in Figure 13, p decreases monotonously with disk temperature. This suggests that the disk evolves from 2022 to 2023 toward a slim one with a decreasing radiation efficiency. Rawat et al. (2023) found that the polarization fraction in the 2023 outburst is lower than that of the 2022 outburst, and thus suggested that the decrease in the polarization fraction could be attributed to the presence of the corona. This is consistent with our finding that the non-thermal emission in the 2023 outburst occupies a fraction larger than that in the 2022 outburst.

Abe et al. (2005) found from a series of outbursts of 4U 1630–472 that, the source can evolve between regimes in the diagram of non-thermal emission fraction against total luminosity. Here two more outbursts in 2022 and 2023 are added to this diagram for further tracing the disk evolution patterns. As shown in Figure 14, the grey dots represent the data points in this article to illustrate the evolution of the luminosity ratio (the non-thermal component to the total) against the total luminosity. The others outburst 5 and outburst 2 defined in Abe et al. (2005) observed by RXTE.

Figure 14 shows that outbursts trace different evolutionary tracks. For outburst 5, the source evolves from HSS into an apparently standard regime and then into the anomalous regime, along with increases in the luminosity and non-thermal fraction. It seems that 4U 1630–472 can stay at HSS with different non-thermal fractions. For example, outburst 2 has an average of

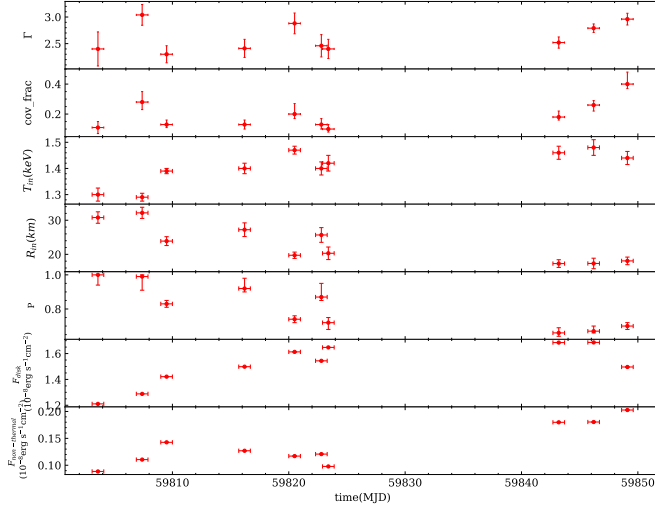


Figure 11. Evolution of the spectral parameters of 4U 1630–472 in 2022 and 2023 from model M3: Γ is the low-energy power-law photon index, T_{in} the temperature of the inner disk, Cov.frac the coverage factor, and R_{in} the inner radius of the disk, p the exponent of the radial dependence of the disk temperature, F_{disk} and $F_{\text{non-thermal}}$ are disk flux and non-thermal flux, respectively. The colors inherit those in Figure 3.

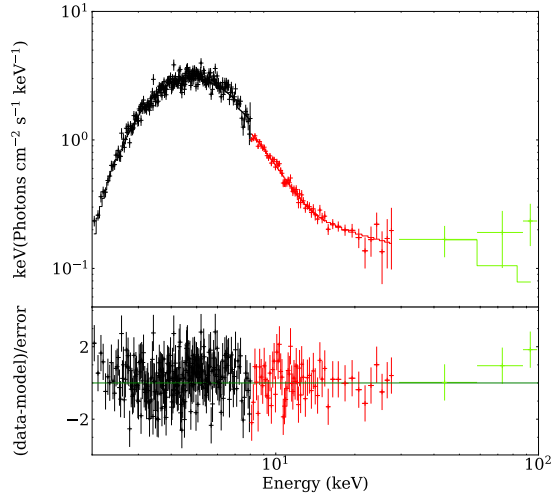


Figure 12. Spectral fit of M3 for 4U 1630–472 of Obs P040426302301. The black, red, and green symbols correspond to the LE, ME, and HE data from Insight-HXMT, respectively.

the non-thermal fraction of around 0.5. It is interesting that in outburst 2 the source evolves almost directly from HSS into the anomalous regime, with less evidence of observing in between an apparently standard pattern (i.e. likely a slim disk or a disk deviating from the standard one). The 2022 and 2023 outbursts are enclosed in Figure 14 and occupy the regimes roughly between outbursts 2 and 5. It looks like that, according to Abe et al. (2005), the 2022 outburst stays in the regime relevant to the standard disk and the 2023 outburst enters into the apparently standard regime. We test our data and Abe et al. (2005) data using the KS-test for the standard

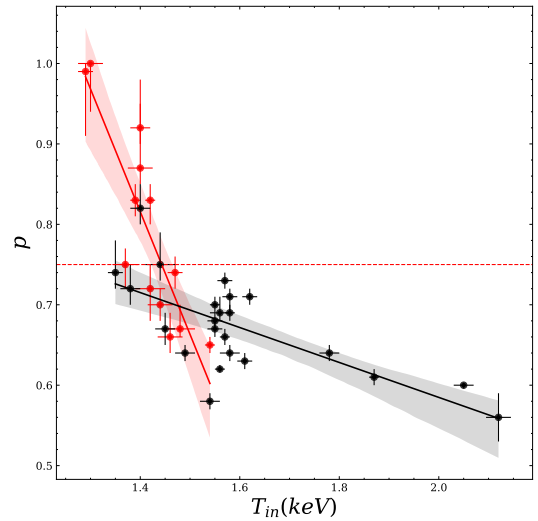
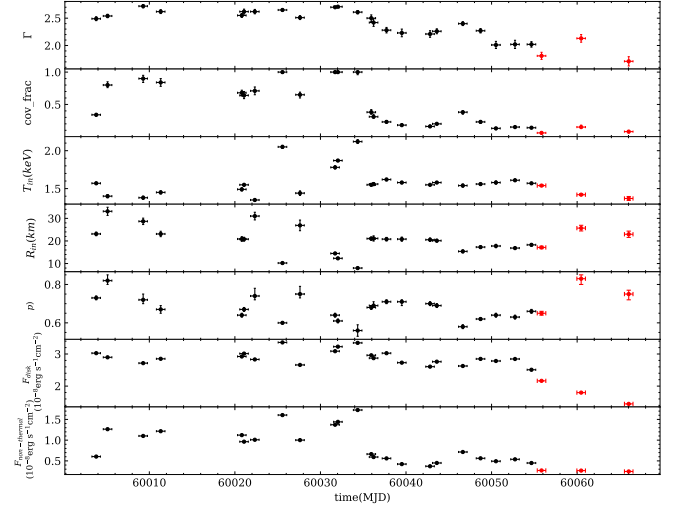


Figure 13. Evolution of p against inner disk temperature T_{in} . Colors inherit those in Figure 3. The grey lines are the fits with linear slopes of -1.53 and -0.22. Shaded areas are 95% confidence intervals.

and apparently regimes. For the standard regime, the KS statistic (d-value) and p-value obtained are 0.17 and 0.98 which is suggestive of the same distribution, while for the apparent regime, the KS statistic and p-value obtained are 0.25 and 0.04 which is not suggestive of the same distribution. We find that the p value in the 2023 outburst is larger than 0.5 required for a slim disk and it evolves significantly in the 2022 and 2023 outbursts in a manner decreasing with luminosity. These findings may suggest that the previously reported apparently standard regime may not be fully relevant to a slim disk but stands for an evolution toward the slim disk. The

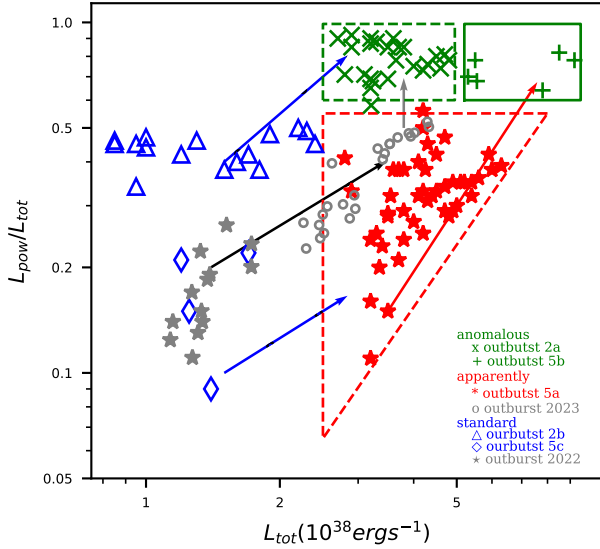


Figure 14. Luminosity ratio of the non-thermal to the total obtained with model M1, plotted against the total luminosity. The green rectangle and red dashed triangle represent the anomalous and apparently standard regimes defined in Abe et al. (2005). The RXTE data with blue triangles and diamonds are relevant to the standard regime Abe et al. (2005). The blue arrows represent the evolution with luminosity in Abe et al. (2005). The grey color represents the data from our article, with the star symbol representing the outburst in 2022 and the dot symbol the outburst in 2023. The black arrow indicates the direction of luminosity evolution, while the grey arrow shows the possible evolving direction at higher luminosities.

formation of a slim disk may be influenced, apart from the accretion rate, as well by the disk/corona properties (e.g. non-thermal fraction) in HSS. A slim disk may be less likely to form with the presence of the dominant non-thermal emission in HSS. The existence of a hot corona may help to ionize the outer part of the disk in the vertical direction and hence hinder the formation of a slim disk by alleviating the optical depth.

1 This work is supported by the National Key R&D
 2 Program of China (2021YFA0718500), the National
 3 Natural Science Foundation of China under grants
 4 No. 12333007, U1838202, U2038101, U1938103,
 5 12273030, U1938107, 12027803 and 12173103. This
 6 work made use of data and software from the Insight-
 7 HXMT mission, a project funded by the China Na-
 8 tional Space Administration (CNSA) and the Chi-
 9 nese Academy of Sciences(CAS). This work was par-
 10 tially supported by the International Partnership Pro-
 11 gram of the Chinese Academy of Sciences (Grant
 12 No.113111KYSB20190020). This research has made use
 13 of software provided by data obtained from the High
 14 Energy Astrophysics Science Archive Research Cen-
 15 ter (HEASARC), provided by NASA’s Goddard Space
 16 Flight Center. L. D. Kong is grateful for the financial
 17 support provided by the Sino-German (CSC-DAAD)
 18 Postdoc Scholarship Program (91839752).

APPENDIX

A. THE SPECTRAL PARAMETER

REFERENCES

- Abe, Y., Fukazawa, Y., Kubota, A., Kasama, D., & Makishima, K. 2005, PASJ, 57, 629, doi: [10.1093/pasj/57.4.629](https://doi.org/10.1093/pasj/57.4.629)
- Abramowicz, M. A., Chen, X., Kato, S., Lasota, J.-P., & Regev, O. 1995, ApJL, 438, L37, doi: [10.1086/187709](https://doi.org/10.1086/187709)
- Abramowicz, M. A., Czerny, B., Lasota, J. P., & Szuszkiewicz, E. 1988, ApJ, 332, 646, doi: [10.1086/166683](https://doi.org/10.1086/166683)
- Belloni, T., Homan, J., Casella, P., et al. 2005, A&A, 440, 207, doi: [10.1051/0004-6361:20042457](https://doi.org/10.1051/0004-6361:20042457)
- Belloni, T. M., Motta, S. E., & Muñoz-Darias, T. 2011, Bulletin of the Astronomical Society of India, 39, 409, doi: [10.48550/arXiv.1109.3388](https://doi.org/10.48550/arXiv.1109.3388)
- Cannizzo, J. K., Chen, W., & Livio, M. 1995, ApJ, 454, 880, doi: [10.1086/176541](https://doi.org/10.1086/176541)
- Cao, X., Jiang, W., Meng, B., et al. 2020, Science China Physics, Mechanics, and Astronomy, 63, 249504, doi: [10.1007/s11433-019-1506-1](https://doi.org/10.1007/s11433-019-1506-1)
- Chen, Y., Cui, W., Li, W., et al. 2020, Science China Physics, Mechanics, and Astronomy, 63, 249505, doi: [10.1007/s11433-019-1469-5](https://doi.org/10.1007/s11433-019-1469-5)
- Chen, Y. P., Zhang, S., Qu, J. L., et al. 2018, ApJL, 864, L30, doi: [10.3847/2041-8213/aadc0e](https://doi.org/10.3847/2041-8213/aadc0e)
- Deegan, P., Combet, C., & Wynn, G. A. 2009, MNRAS, 400, 1337, doi: [10.1111/j.1365-2966.2009.15573.x](https://doi.org/10.1111/j.1365-2966.2009.15573.x)
- Esin, A. A., McClintock, J. E., & Narayan, R. 1997, ApJ, 489, 865, doi: [10.1086/304829](https://doi.org/10.1086/304829)
- Giacconi, R., Murray, S., Gursky, H., et al. 1972, ApJ, 178, 281, doi: [10.1086/151790](https://doi.org/10.1086/151790)

Table 1. Fitting results of Insight-HXMT for Model M1. Γ is the low-energy power-law photon index, T_{in} the temperature of the inner disk, Cov_frac the coverage factor, and r_{in} the inner radius of the disk. F_{disk} and $F_{\text{non-thermal}}$ are disk flux and non-thermal flux, respectively.

Insight-HXMT ObsID	MJD	Γ	Cov_frac	T_{in} (keV)	r_{in} (km)	F_{disk} (10^{-8} erg s $^{-1}$ cm $^{-2}$)	$F_{\text{non-thermal}}$ (10^{-8} erg s $^{-1}$ cm $^{-2}$)	χ^2/dof
P040426302301	59803.6	$2.13^{+0.37}_{-0.13}$	$0.07^{+0.04}_{-0.01}$	$1.42^{+0.02}_{-0.02}$	$20.15^{+4.81}_{-4.59}$	$1.33^{+0.02}_{-0.02}$	$0.10^{+0.03}_{-0.03}$	942/895
P040426302403	59807.4	$2.76^{+0.08}_{-0.2}$	$0.19^{+0.08}_{-0.04}$	$1.39^{+0.02}_{-0.03}$	$20.98^{+5.81}_{-4.66}$	$1.41^{+0.02}_{-0.02}$	$0.11^{+0.02}_{-0.02}$	937/895
P040426302501	59809.5	$2.18^{+0.17}_{-0.15}$	$0.11^{+0.03}_{-0.02}$	$1.44^{+0.01}_{-0.01}$	$20.17^{+3.89}_{-3.98}$	$1.48^{+0.02}_{-0.02}$	$0.15^{+0.03}_{-0.02}$	931/895
P040426302701	59816.2	$2.11^{+0.18}_{-0.18}$	$0.08^{+0.03}_{-0.02}$	$1.49^{+0.01}_{-0.02}$	$19.54^{+4.10}_{-2.92}$	$1.61^{+0.01}_{-0.01}$	$0.14^{+0.02}_{-0.02}$	893/895
P040426302802	59820.5	$2.93^{+0.3}_{-0.05}$	$0.21^{+0.09}_{-0.05}$	$1.46^{+0.01}_{-0.02}$	$20.40^{+4.27}_{-4.04}$	$1.60^{+0.01}_{-0.01}$	$0.12^{+0.02}_{-0.02}$	872/895
P040426302901	59822.8	$2.15^{+0.28}_{-0.33}$	$0.08^{+0.03}_{-0.03}$	$1.48^{+0.03}_{-0.01}$	$19.98^{+4.04}_{-5.26}$	$1.63^{+0.02}_{-0.02}$	$0.13^{+0.04}_{-0.03}$	828/895
P040426303001	59823.4	$2.60^{+0.26}_{-0.29}$	$0.12^{+0.04}_{-0.03}$	$1.39^{+0.01}_{-0.01}$	$22.44^{+3.95}_{-4.27}$	$1.61^{+0.01}_{-0.01}$	$0.10^{+0.01}_{-0.01}$	969/895
P051435300101	59843.2	$2.73^{+0.16}_{-0.09}$	$0.25^{+0.07}_{-0.03}$	$1.37^{+0.02}_{-0.01}$	$22.99^{+4.61}_{-5.10}$	$1.57^{+0.01}_{-0.01}$	$0.18^{+0.02}_{-0.02}$	908/895
P051435300301	59846.2	$3.01^{+0.11}_{-0.14}$	$0.36^{+0.05}_{-0.05}$	$1.39^{+0.01}_{-0.01}$	$22.39^{+4.29}_{-4.07}$	$1.58^{+0.01}_{-0.01}$	$0.18^{+0.01}_{-0.01}$	1023/895
P051435300401	59849.1	$3.06^{+0.11}_{-0.1}$	$0.46^{+0.07}_{-0.06}$	$1.39^{+0.01}_{-0.02}$	$21.42^{+4.64}_{-3.86}$	$1.44^{+0.01}_{-0.01}$	$0.20^{+0.01}_{-0.01}$	968/895
P050523700101	60003.8	$2.51^{+0.05}_{-0.05}$	$0.35^{+0.03}_{-0.02}$	$1.55^{+0.01}_{-0.01}$	$24.51^{+3.77}_{-3.67}$	$2.99^{+0.01}_{-0.01}$	$0.60^{+0.01}_{-0.01}$	810/895
P050523700201	60005.1	$2.53^{+0.04}_{-0.04}$	$0.77^{+0.06}_{-0.06}$	$1.45^{+0.03}_{-0.03}$	$27.94^{+7.84}_{-7.36}$	$2.96^{+0.07}_{-0.07}$	$1.29^{+0.08}_{-0.08}$	926/895
P050523700402	60009.3	$2.73^{+0.03}_{-0.03}$	$0.92^{+0.06}_{-0.05}$	$1.36^{+0.03}_{-0.02}$	$30.71^{+8.05}_{-8.29}$	$2.69^{+0.02}_{-0.02}$	$1.10^{+0.03}_{-0.03}$	833/895
P050523700501	60011.3	$2.66^{+0.07}_{-0.04}$	$0.91^{+0.07}_{-0.04}$	$1.35^{+0.02}_{-0.03}$	$31.25^{+8.82}_{-7.06}$	$2.72^{+0.02}_{-0.02}$	$1.19^{+0.02}_{-0.03}$	859/895
P050523700901	60020.8	$2.62^{+0.03}_{-0.03}$	$0.80^{+0.07}_{-0.04}$	$1.34^{+0.02}_{-0.02}$	$31.65^{+8.31}_{-6.84}$	$2.72^{+0.01}_{-0.01}$	$1.10^{+0.02}_{-0.02}$	804/895
P050523700903	60021.1	$2.71^{+0.04}_{-0.04}$	$0.75^{+0.06}_{-0.05}$	$1.43^{+0.01}_{-0.02}$	$28.35^{+5.50}_{-5.61}$	$2.85^{+0.01}_{-0.01}$	$0.96^{+0.02}_{-0.02}$	866/895
P050523701102	60022.3	$2.62^{+0.04}_{-0.06}$	$0.71^{+0.06}_{-0.08}$	$1.34^{+0.04}_{-0.02}$	$32.00^{+8.39}_{-10.08}$	$2.82^{+0.03}_{-0.03}$	$1.01^{+0.05}_{-0.05}$	935/895
P050523701302	60025.6	$2.61^{+0.01}_{-0.01}$	$1.00^{+0.0}_{-0.01}$	$1.65^{+0.01}_{-0.01}$	$21.95^{+2.96}_{-4.13}$	$3.06^{+0.01}_{-0.01}$	$1.51^{+0.02}_{-0.02}$	1104/895
P050523701402	60027.6	$2.51^{+0.05}_{-0.03}$	$0.65^{+0.07}_{-0.03}$	$1.44^{+0.02}_{-0.03}$	$26.89^{+7.50}_{-8.92}$	$2.66^{+0.02}_{-0.02}$	$1.00^{+0.03}_{-0.03}$	904/895
P050523701701	60031.7	$2.70^{+0.01}_{-0.01}$	$1.00^{+0.0}_{-0.01}$	$1.57^{+0.01}_{-0.01}$	$23.50^{+3.61}_{-4.21}$	$2.91^{+0.01}_{-0.01}$	$1.30^{+0.01}_{-0.01}$	1026/895
P050523701703	60032.0	$2.69^{+0.01}_{-0.01}$	$1.00^{+0.0}_{-0.02}$	$1.56^{+0.01}_{-0.01}$	$24.12^{+4.10}_{-4.35}$	$2.97^{+0.01}_{-0.01}$	$1.35^{+0.02}_{-0.02}$	1021/895
P050523701802	60034.4	$2.57^{+0.04}_{-0.01}$	$1.00^{+0.0}_{-0.02}$	$1.52^{+0.01}_{-0.01}$	$25.31^{+4.18}_{-4.04}$	$2.92^{+0.01}_{-0.01}$	$1.54^{+0.02}_{-0.02}$	1111/895
P050523701901	60035.9	$2.61^{+0.07}_{-0.05}$	$0.46^{+0.06}_{-0.04}$	$1.46^{+0.01}_{-0.02}$	$27.02^{+5.79}_{-5.03}$	$2.81^{+0.01}_{-0.01}$	$0.65^{+0.02}_{-0.02}$	893/895
P050523701903	60036.2	$2.51^{+0.06}_{-0.08}$	$0.37^{+0.03}_{-0.04}$	$1.48^{+0.01}_{-0.02}$	$25.89^{+5.19}_{-4.94}$	$2.75^{+0.01}_{-0.01}$	$0.58^{+0.02}_{-0.02}$	870/895
P050523702001	60037.7	$2.35^{+0.05}_{-0.05}$	$0.26^{+0.02}_{-0.02}$	$1.57^{+0.01}_{-0.01}$	$23.85^{+3.08}_{-3.26}$	$2.94^{+0.01}_{-0.01}$	$0.55^{+0.01}_{-0.01}$	933/895
P050523702101	60039.5	$2.29^{+0.06}_{-0.05}$	$0.20^{+0.02}_{-0.02}$	$1.54^{+0.01}_{-0.01}$	$23.49^{+3.70}_{-3.26}$	$2.66^{+0.01}_{-0.01}$	$0.41^{+0.02}_{-0.02}$	882/895
P050523702201	60042.8	$2.29^{+0.07}_{-0.05}$	$0.18^{+0.02}_{-0.01}$	$1.50^{+0.01}_{-0.01}$	$24.13^{+2.92}_{-2.92}$	$2.51^{+0.01}_{-0.01}$	$0.36^{+0.02}_{-0.02}$	911/895
P050523702301	60043.6	$2.35^{+0.01}_{-0.06}$	$0.23^{+0.01}_{-0.01}$	$1.52^{+0.01}_{-0.01}$	$24.22^{+2.75}_{-3.89}$	$2.65^{+0.01}_{-0.01}$	$0.43^{+0.01}_{-0.01}$	869/895
P050523702402	60046.6	$2.63^{+0.02}_{-0.03}$	$0.63^{+0.02}_{-0.03}$	$1.27^{+0.01}_{-0.01}$	$31.79^{+5.69}_{-5.81}$	$2.23^{+0.01}_{-0.01}$	$0.72^{+0.02}_{-0.01}$	1175/895
P050523702501	60048.7	$2.47^{+0.03}_{-0.02}$	$0.34^{+0.02}_{-0.01}$	$1.39^{+0.01}_{-0.01}$	$28.26^{+4.21}_{-3.30}$	$2.53^{+0.01}_{-0.01}$	$0.53^{+0.01}_{-0.01}$	1225/895
P050523702601	60050.5	$2.20^{+0.06}_{-0.06}$	$0.19^{+0.02}_{-0.02}$	$1.45^{+0.01}_{-0.01}$	$26.04^{+3.89}_{-4.59}$	$2.53^{+0.01}_{-0.01}$	$0.45^{+0.02}_{-0.02}$	1014/895
P050523702701	60052.7	$2.25^{+0.07}_{-0.06}$	$0.23^{+0.02}_{-0.02}$	$1.45^{+0.01}_{-0.01}$	$25.95^{+4.32}_{-4.40}$	$2.55^{+0.01}_{-0.01}$	$0.49^{+0.02}_{-0.02}$	1136/895
P050523703301	60054.7	$2.16^{+0.02}_{-0.07}$	$0.18^{+0.01}_{-0.02}$	$1.47^{+0.01}_{-0.01}$	$24.26^{+2.53}_{-3.83}$	$2.34^{+0.01}_{-0.01}$	$0.42^{+0.01}_{-0.01}$	967/895
P050523703401	60055.8	$2.00^{+0.08}_{-0.09}$	$0.09^{+0.01}_{-0.01}$	$1.43^{+0.01}_{-0.01}$	$23.41^{+3.19}_{-3.23}$	$1.99^{+0.01}_{-0.01}$	$0.24^{+0.02}_{-0.02}$	938/895
P050523703602	60060.5	$2.05^{+0.10}_{-0.10}$	$0.13^{+0.02}_{-0.02}$	$1.47^{+0.01}_{-0.01}$	$21.71^{+3.87}_{-3.83}$	$1.87^{+0.01}_{-0.01}$	$0.28^{+0.02}_{-0.02}$	918/895
P050523703901	60066.0	$1.62^{+0.17}_{-0.09}$	$0.01^{+0.02}_{-0.01}$	$1.36^{+0.02}_{-0.03}$	$23.29^{+7.42}_{-6.61}$	$1.58^{+0.08}_{-0.08}$	$0.28^{+0.12}_{-0.09}$	912/895

Goodman, J., & Weare, J. 2010, Communications in Applied Mathematics and Computational Science, 5, 65, doi: [10.2140/camcos.2010.5.65](https://doi.org/10.2140/camcos.2010.5.65)

Hirano, A., Kitamoto, S., Yamada, T. T., Mineshige, S., & Fukue, J. 1995, ApJ, 446, 350, doi: [10.1086/175793](https://doi.org/10.1086/175793)

Jones, C., Forman, W., Tananbaum, H., & Turner, M. J. L. 1976, ApJL, 210, L9, doi: [10.1086/182291](https://doi.org/10.1086/182291)

Kalemci, E., Maccarone, T. J., & Tomsick, J. A. 2018, ApJ, 859, 88, doi: [10.3847/1538-4357/aabcd3](https://doi.org/10.3847/1538-4357/aabcd3)

King, A. L., Walton, D. J., Miller, J. M., et al. 2014, ApJL, 784, L2, doi: [10.1088/2041-8205/784/1/L2](https://doi.org/10.1088/2041-8205/784/1/L2)

Kubota, A., & Makishima, K. 2004, ApJ, 601, 428, doi: [10.1086/380433](https://doi.org/10.1086/380433)

Kubota, A., Tanaka, Y., Makishima, K., et al. 1998, PASJ, 50, 667, doi: [10.1093/pasj/50.6.667](https://doi.org/10.1093/pasj/50.6.667)

Kuulkers, E., Parmar, A. N., Kitamoto, S., Cominsky, L. R., & Sood, R. K. 1997, MNRAS, 291, 81, doi: [10.1093/mnras/291.1.81](https://doi.org/10.1093/mnras/291.1.81)

Kuulkers, E., Wijnands, R., Belloni, T., et al. 1998, ApJ, 494, 753, doi: [10.1086/305248](https://doi.org/10.1086/305248)

Kylafis, N. D., & Belloni, T. M. 2015, A&A, 574, A133, doi: [10.1051/0004-6361/201425106](https://doi.org/10.1051/0004-6361/201425106)

Lasota, J.-P. 2001, NewAR, 45, 449, doi: [10.1016/S1387-6473\(01\)00112-9](https://doi.org/10.1016/S1387-6473(01)00112-9)

Liao, J.-Y., Zhang, S., Lu, X.-F., et al. 2020, Journal of High Energy Astrophysics, 27, 14, doi: [10.1016/j.jheap.2020.04.002](https://doi.org/10.1016/j.jheap.2020.04.002)

Table 2. Fitting results of Insight-HXMT for Model M2. Γ is the low-energy power-law photon index, Cov_frac the coverage factor, M_{dd} the “effective” mass accretion rate of the disk in units of 10^{18} g/s, f_{col} the spectral hardening factor and T_{eff} the effective temperature of the inner zone of the disk, obtained by $T_{\text{in}}/f_{\text{col}}$, and R_{in} the inner radius of the disk.

Insight-HXMT ObsID	MJD	Γ	Cov_frac	M_{dd}	f_{col}	T_{eff} (keV)	R_{in} (km)	χ^2/dof
P040426302301	59803.6	$1.78^{+0.27}_{-0.24}$	$0.04^{+0.02}_{-0.01}$	$1.62^{+0.02}_{-0.02}$	$1.78^{+0.79}_{-0.03}$	$0.80^{+0.02}_{-0.02}$	$26.17^{+0.79}_{-0.73}$	996/896
P040426302403	59807.4	$2.40^{+0.31}_{-0.28}$	$0.10^{+0.05}_{-0.03}$	$1.71^{+0.02}_{-0.02}$	$1.76^{+1.07}_{-0.03}$	$0.79^{+0.02}_{-0.02}$	$26.64^{+1.07}_{-0.71}$	977/896
P040426302501	59809.5	$1.84^{+0.19}_{-0.17}$	$0.06^{+0.02}_{-0.01}$	$1.79^{+0.01}_{-0.01}$	$1.8^{+0.52}_{-0.02}$	$0.8^{+0.01}_{-0.01}$	$26.795^{+0.52}_{-0.543}$	1021/896
P040426302701	59816.2	$1.63^{+0.23}_{-0.21}$	$0.03^{+0.01}_{-0.01}$	$1.94^{+0.01}_{-0.01}$	$1.84^{+0.62}_{-0.02}$	$0.81^{+0.01}_{-0.01}$	$27.12^{+0.62}_{-0.32}$	1034/896
P040426302802	59820.5	$2.19^{+0.40}_{-0.30}$	$0.06^{+0.04}_{-0.02}$	$1.94^{+0.01}_{-0.02}$	$1.82^{+0.63}_{-0.02}$	$0.80^{+0.01}_{-0.01}$	$27.71^{+0.63}_{-0.57}$	920/896
P040426302901	59822.8	$1.52^{+0.41}_{-0.33}$	$0.03^{+0.02}_{-0.01}$	$1.98^{+0.02}_{-0.02}$	$1.83^{+0.61}_{-0.03}$	$0.81^{+0.02}_{-0.01}$	$27.43^{+0.61}_{-1.00}$	869/896
P040426303001	59823.4	$1.90^{+0.28}_{-0.26}$	$0.04^{+0.02}_{-0.01}$	$1.97^{+0.01}_{-0.01}$	$1.71^{+0.42}_{-0.01}$	$0.81^{+0.01}_{-0.01}$	$26.90^{+0.42}_{-0.49}$	1020/896
P051435300101	59843.2	$2.37^{+0.16}_{-0.15}$	$0.14^{+0.04}_{-0.03}$	$1.91^{+0.01}_{-0.02}$	$1.69^{+0.56}_{-0.02}$	$0.81^{+0.02}_{-0.01}$	$26.92^{+0.56}_{-0.68}$	898/896
P051435300301	59846.2	$2.57^{+0.15}_{-0.14}$	$0.17^{+0.04}_{-0.03}$	$1.93^{+0.01}_{-0.02}$	$1.73^{+0.53}_{-0.02}$	$0.80^{+0.01}_{-0.01}$	$27.47^{+0.53}_{-0.48}$	1000/896
P051435300401	59849.1	$2.75^{+0.15}_{-0.15}$	$0.27^{+0.06}_{-0.05}$	$1.74^{+0.01}_{-0.02}$	$1.77^{+0.67}_{-0.02}$	$0.79^{+0.01}_{-0.01}$	$27.52^{+0.67}_{-0.47}$	962/896
P050523700101	60003.8	$2.30^{+0.06}_{-0.04}$	$0.24^{+0.02}_{-0.01}$	$3.50^{+0.01}_{-0.02}$	$1.68^{+0.34}_{-0.01}$	$0.92^{+0.01}_{-0.01}$	$28.37^{+0.34}_{-0.32}$	931/896
P050523700201	60005.1	$2.50^{+0.05}_{-0.04}$	$0.69^{+0.06}_{-0.05}$	$3.41^{+0.04}_{-0.04}$	$1.55^{+1.13}_{-0.04}$	$0.94^{+0.03}_{-0.03}$	$27.52^{+1.13}_{-1.04}$	942/896
P050523700402	60009.3	$2.70^{+0.04}_{-0.04}$	$0.78^{+0.07}_{-0.06}$	$3.13^{+0.05}_{-0.05}$	$1.49^{+1.01}_{-0.03}$	$0.91^{+0.03}_{-0.02}$	$27.95^{+1.01}_{-1.07}$	839/896
P050523700501	60011.3	$2.60^{+0.04}_{-0.03}$	$0.78^{+0.07}_{-0.05}$	$3.16^{+0.03}_{-0.04}$	$1.47^{+1.15}_{-0.03}$	$0.92^{+0.02}_{-0.03}$	$27.69^{+1.15}_{-0.76}$	827/896
P050523700901	60020.8	$2.54^{+0.03}_{-0.03}$	$0.64^{+0.05}_{-0.05}$	$3.20^{+0.03}_{-0.03}$	$1.46^{+0.98}_{-0.02}$	$0.92^{+0.02}_{-0.02}$	$27.66^{+0.98}_{-0.67}$	752/896
P050523700903	60021.1	$2.57^{+0.06}_{-0.05}$	$0.55^{+0.06}_{-0.04}$	$3.36^{+0.03}_{-0.03}$	$1.57^{+0.56}_{-0.02}$	$0.91^{+0.01}_{-0.02}$	$28.65^{+0.56}_{-0.58}$	826/896
P050523701102	60022.3	$2.55^{+0.04}_{-0.05}$	$0.68^{+0.07}_{-0.06}$	$3.16^{+0.04}_{-0.04}$	$1.49^{+1.05}_{-0.03}$	$0.90^{+0.03}_{-0.02}$	$29.13^{+1.05}_{-1.50}$	928/896
P050523701302	60025.6	$2.64^{+0.02}_{-0.01}$	$1.00^{+0.00}_{-0.03}$	$3.38^{+0.02}_{-0.01}$	$1.78^{+0.28}_{-0.01}$	$0.93^{+0.01}_{-0.01}$	$28.51^{+0.28}_{-0.51}$	872/896
P050523701402	60027.6	$2.45^{+0.05}_{-0.05}$	$0.56^{+0.05}_{-0.05}$	$3.10^{+0.03}_{-0.03}$	$1.58^{+1.12}_{-0.03}$	$0.91^{+0.02}_{-0.03}$	$27.52^{+1.12}_{-0.63}$	911/896
P050523701701	60031.7	$2.72^{+0.01}_{-0.02}$	$1.00^{+0.00}_{-0.04}$	$3.22^{+0.02}_{-0.01}$	$1.70^{+0.35}_{-0.01}$	$0.92^{+0.01}_{-0.01}$	$27.84^{+0.35}_{-0.45}$	857/896
P050523701703	60032.0	$2.72^{+0.01}_{-0.02}$	$1.00^{+0.00}_{-0.03}$	$3.29^{+0.02}_{-0.01}$	$1.68^{+0.43}_{-0.01}$	$0.93^{+0.01}_{-0.01}$	$27.91^{+0.43}_{-0.46}$	886/896
P050523701802	60034.4	$2.59^{+0.01}_{-0.05}$	$1.00^{+0.00}_{-0.03}$	$3.24^{+0.03}_{-0.01}$	$1.63^{+0.43}_{-0.01}$	$0.93^{+0.02}_{-0.01}$	$27.57^{+0.43}_{-0.36}$	899/896
P050523701901	60035.9	$2.39^{+0.08}_{-0.05}$	$0.30^{+0.03}_{-0.03}$	$3.35^{+0.02}_{-0.02}$	$1.60^{+0.66}_{-0.02}$	$0.91^{+0.01}_{-0.02}$	$28.36^{+0.66}_{-0.51}$	882/896
P050523701903	60036.2	$2.28^{+0.11}_{-0.08}$	$0.24^{+0.04}_{-0.03}$	$3.28^{+0.02}_{-0.04}$	$1.62^{+0.58}_{-0.02}$	$0.91^{+0.01}_{-0.02}$	$27.86^{+0.58}_{-0.53}$	878/896
P050523702001	60037.7	$2.06^{+0.06}_{-0.05}$	$0.15^{+0.01}_{-0.01}$	$3.49^{+0.01}_{-0.01}$	$1.70^{+0.241}_{-0.01}$	$0.92^{+0.01}_{-0.01}$	$28.26^{+0.24}_{-0.27}$	1045/896
P050523702101	60039.5	$2.03^{+0.07}_{-0.07}$	$0.12^{+0.01}_{-0.01}$	$3.17^{+0.01}_{-0.01}$	$1.70^{+0.35}_{-0.01}$	$0.91^{+0.01}_{-0.01}$	$27.83^{+0.35}_{-0.27}$	1087/896
P050523702201	60042.8	$2.05^{+0.08}_{-0.06}$	$0.12^{+0.02}_{-0.01}$	$3.01^{+0.01}_{-0.01}$	$1.66^{+0.21}_{-0.01}$	$0.90^{+0.01}_{-0.01}$	$27.26^{+0.21}_{-0.21}$	1007/896
P050523702301	60043.6	$2.09^{+0.05}_{-0.06}$	$0.14^{+0.01}_{-0.01}$	$3.16^{+0.01}_{-0.01}$	$1.67^{+0.18}_{-0.01}$	$0.91^{+0.01}_{-0.01}$	$27.69^{+0.18}_{-0.36}$	1007/896
P050523702402	60046.6	$2.46^{+0.04}_{-0.03}$	$0.42^{+0.03}_{-0.02}$	$2.70^{+0.01}_{-0.02}$	$1.47^{+0.46}_{-0.01}$	$0.86^{+0.01}_{-0.01}$	$28.16^{+0.46}_{-0.48}$	925/896
P050523702501	60048.7	$2.28^{+0.04}_{-0.05}$	$0.23^{+0.02}_{-0.02}$	$3.04^{+0.01}_{-0.01}$	$1.53^{+0.31}_{-0.01}$	$0.91^{+0.01}_{-0.01}$	$27.12^{+0.31}_{-0.19}$	1042/896
P050523702601	60050.5	$1.96^{+0.09}_{-0.05}$	$0.12^{+0.02}_{-0.01}$	$3.04^{+0.01}_{-0.02}$	$1.60^{+0.31}_{-0.01}$	$0.91^{+0.01}_{-0.01}$	$27.33^{+0.31}_{-0.43}$	960/896
P050523702701	60052.7	$2.00^{+0.06}_{-0.06}$	$0.14^{+0.01}_{-0.01}$	$3.07^{+0.01}_{-0.01}$	$1.61^{+0.39}_{-0.01}$	$0.90^{+0.01}_{-0.01}$	$27.58^{+0.39}_{-0.40}$	1003/896
P050523703301	60054.7	$1.93^{+0.06}_{-0.05}$	$0.12^{+0.01}_{-0.01}$	$2.81^{+0.01}_{-0.01}$	$1.66^{+0.15}_{-0.01}$	$0.89^{+0.01}_{-0.01}$	$27.41^{+0.15}_{-0.35}$	991/896
P050523703401	60055.8	$1.72^{+0.10}_{-0.08}$	$0.05^{+0.01}_{-0.00}$	$2.41^{+0.01}_{-0.01}$	$1.67^{+0.25}_{-0.01}$	$0.86^{+0.01}_{-0.01}$	$26.77^{+0.25}_{-0.26}$	916/896
P050523703602	60060.5	$1.85^{+0.10}_{-0.09}$	$0.09^{+0.01}_{-0.01}$	$2.25^{+0.01}_{-0.01}$	$1.74^{+0.39}_{-0.02}$	$0.85^{+0.01}_{-0.01}$	$26.94^{+0.39}_{-0.44}$	1052/896
P050523703901	60066.0	$1.50^{+0.18}_{-0.12}$	$0.05^{+0.01}_{-0.01}$	$1.94^{+0.03}_{-0.03}$	$1.63^{+1.37}_{-0.04}$	$0.83^{+0.02}_{-0.03}$	$25.37^{+1.37}_{-1.10}$	945/896

Liu, C., Zhang, Y., Li, X., et al. 2020, Science China Physics, Mechanics, and Astronomy, 63, 249503, doi: [10.1007/s11433-019-1486-x](https://doi.org/10.1007/s11433-019-1486-x)

Liu, Q., Liu, H., Bambi, C., & Ji, L. 2022, MNRAS, 512, 2082, doi: [10.1093/mnras/stac616](https://doi.org/10.1093/mnras/stac616)

Ma, R. C., Soria, R., Tao, L., et al. 2022, MNRAS, 514, 5238, doi: [10.1093/mnras/stac1585](https://doi.org/10.1093/mnras/stac1585)

Madej, J. 1974, AcA, 24, 327

Makishima, K., Kubota, A., Mizuno, T., et al. 2000, ApJ, 535, 632, doi: [10.1086/308868](https://doi.org/10.1086/308868)

Merloni, A., Fabian, A. C., & Ross, R. R. 2000, MNRAS, 313, 193, doi: [10.1046/j.1365-8711.2000.03226.x](https://doi.org/10.1046/j.1365-8711.2000.03226.x)

Mineshige, S., Hirano, A., Kitamoto, S., Yamada, T. T., & Fukue, J. 1994, ApJ, 426, 308, doi: [10.1086/174065](https://doi.org/10.1086/174065)

Mitsuda, K., Inoue, H., Koyama, K., et al. 1984, PASJ, 36, 741

Table 3. Fitting results of Insight-HXMT for Model M3. Γ is the low-energy power-law photon index, T_{in} the temperature of the inner disk, Cov_frac the coverage factor, and R_{in} the inner radius of the disk, p the exponent of the radial dependence of the disk temperature, F_{disk} and $F_{\text{non-thermal}}$ are disk flux and non-thermal flux, respectively.

Insight-HXMT ObsID	MJD	Γ	Cov_frac	T_{in} (keV)	R_{in} (km)	p	F_{disk} (10^{-8} erg s $^{-1}$ cm $^{-2}$)	$F_{\text{non-thermal}}$ (10^{-8} erg s $^{-1}$ cm $^{-2}$)	χ^2/dof
P040426302301	59803.6	2.40 $^{+0.26}_{-0.38}$	0.11 $^{+0.04}_{-0.04}$	1.30 $^{+0.03}_{-0.02}$	30.79 $^{+5.04}_{-13.47}$	1.00 $^{+0.00}_{-0.06}$	1.21 $^{+0.01}_{-0.01}$	0.09 $^{+0.02}_{-0.02}$	935/894
P040426302403	59807.4	3.04 $^{+0.23}_{-0.16}$	0.28 $^{+0.07}_{-0.05}$	1.29 $^{+0.02}_{-0.01}$	32.17 $^{+6.65}_{-12.89}$	0.99 $^{+0.01}_{-0.08}$	1.29 $^{+0.02}_{-0.02}$	0.11 $^{+0.02}_{-0.02}$	929/894
P040426302501	59809.5	2.30 $^{+0.17}_{-0.15}$	0.13 $^{+0.03}_{-0.02}$	1.39 $^{+0.01}_{-0.01}$	23.88 $^{+8.29}_{-7.42}$	0.83 $^{+0.02}_{-0.02}$	1.42 $^{+0.02}_{-0.02}$	0.14 $^{+0.03}_{-0.02}$	925/894
P040426302701	59816.2	2.41 $^{+0.15}_{-0.19}$	0.13 $^{+0.03}_{-0.03}$	1.40 $^{+0.02}_{-0.02}$	27.22 $^{+12.12}_{-8.46}$	0.92 $^{+0.06}_{-0.02}$	1.50 $^{+0.01}_{-0.01}$	0.13 $^{+0.02}_{-0.02}$	872/894
P040426302802	59820.5	2.88 $^{+0.28}_{-0.11}$	0.20 $^{+0.07}_{-0.04}$	1.47 $^{+0.01}_{-0.02}$	19.73 $^{+6.77}_{-5.19}$	0.74 $^{+0.02}_{-0.02}$	1.61 $^{+0.01}_{-0.01}$	0.12 $^{+0.02}_{-0.02}$	872/894
P040426302901	59822.8	2.46 $^{+0.21}_{-0.21}$	0.13 $^{+0.04}_{-0.03}$	1.40 $^{+0.02}_{-0.03}$	25.68 $^{+12.97}_{-7.33}$	0.87 $^{+0.08}_{-0.02}$	1.54 $^{+0.01}_{-0.01}$	0.12 $^{+0.03}_{-0.02}$	824/894
P040426303001	59823.4	2.40 $^{+0.20}_{-0.16}$	0.10 $^{+0.03}_{-0.02}$	1.42 $^{+0.04}_{-0.01}$	20.31 $^{+8.25}_{-9.01}$	0.72 $^{+0.03}_{-0.04}$	1.65 $^{+0.01}_{-0.01}$	0.10 $^{+0.02}_{-0.02}$	965/894
P051435300101	59843.2	2.52 $^{+0.14}_{-0.07}$	0.18 $^{+0.04}_{-0.02}$	1.46 $^{+0.02}_{-0.02}$	17.29 $^{+7.21}_{-5.10}$	0.66 $^{+0.03}_{-0.02}$	1.69 $^{+0.01}_{-0.01}$	0.18 $^{+0.02}_{-0.02}$	895/894
P051435300301	59846.2	2.79 $^{+0.07}_{-0.09}$	0.26 $^{+0.03}_{-0.04}$	1.48 $^{+0.02}_{-0.04}$	17.33 $^{+9.07}_{-4.94}$	0.67 $^{+0.03}_{-0.01}$	1.69 $^{+0.01}_{-0.01}$	0.18 $^{+0.01}_{-0.01}$	999/894
P051435300401	59849.1	2.96 $^{+0.15}_{-0.07}$	0.40 $^{+0.08}_{-0.03}$	1.44 $^{+0.02}_{-0.03}$	18.08 $^{+6.82}_{-5.84}$	0.70 $^{+0.02}_{-0.02}$	1.50 $^{+0.01}_{-0.01}$	0.20 $^{+0.01}_{-0.01}$	962/894
P050523700101	60003.8	2.49 $^{+0.04}_{-0.03}$	0.34 $^{+0.02}_{-0.02}$	1.57 $^{+0.01}_{-0.02}$	23.11 $^{+6.34}_{-5.75}$	0.73 $^{+0.01}_{-0.01}$	3.03 $^{+0.01}_{-0.03}$	0.60 $^{+0.01}_{-0.01}$	808/894
P050523700201	60005.1	2.54 $^{+0.04}_{-0.02}$	0.80 $^{+0.05}_{-0.02}$	1.40 $^{+0.02}_{-0.02}$	33.11 $^{+11.91}_{-9.85}$	0.82 $^{+0.03}_{-0.02}$	2.90 $^{+0.03}_{-0.03}$	1.26 $^{+0.04}_{-0.04}$	924/894
P050523700402	60009.3	2.72 $^{+0.03}_{-0.03}$	0.90 $^{+0.05}_{-0.06}$	1.38 $^{+0.02}_{-0.02}$	28.68 $^{+9.72}_{-8.21}$	0.72 $^{+0.03}_{-0.02}$	2.72 $^{+0.02}_{-0.02}$	1.10 $^{+0.03}_{-0.03}$	833/894
P050523700501	60011.3	2.62 $^{+0.03}_{-0.03}$	0.84 $^{+0.06}_{-0.06}$	1.45 $^{+0.02}_{-0.02}$	23.10 $^{+7.76}_{-7.06}$	0.67 $^{+0.02}_{-0.02}$	2.85 $^{+0.02}_{-0.02}$	1.22 $^{+0.03}_{-0.03}$	848/894
P050523700901	60020.8	2.55 $^{+0.04}_{-0.04}$	0.68 $^{+0.04}_{-0.05}$	1.49 $^{+0.01}_{-0.01}$	20.87 $^{+6.21}_{-6.84}$	0.64 $^{+0.01}_{-0.01}$	2.92 $^{+0.01}_{-0.01}$	1.12 $^{+0.02}_{-0.02}$	764/894
P050523700903	60021.1	2.62 $^{+0.05}_{-0.04}$	0.64 $^{+0.06}_{-0.05}$	1.55 $^{+0.02}_{-0.01}$	20.78 $^{+5.63}_{-6.21}$	0.67 $^{+0.01}_{-0.01}$	3.01 $^{+0.01}_{-0.01}$	0.96 $^{+0.02}_{-0.02}$	840/894
P050523701102	60022.3	2.62 $^{+0.04}_{-0.04}$	0.71 $^{+0.06}_{-0.06}$	1.35 $^{+0.01}_{-0.02}$	31.01 $^{+11.22}_{-9.20}$	0.74 $^{+0.04}_{-0.02}$	2.83 $^{+0.03}_{-0.03}$	1.01 $^{+0.05}_{-0.05}$	935/894
P050523701302	60025.6	2.65 $^{+0.01}_{-0.02}$	1.00 $^{+0.00}_{-0.02}$	2.05 $^{+0.02}_{-0.02}$	10.22 $^{+2.28}_{-2.28}$	0.60 $^{+0.01}_{-0.01}$	3.36 $^{+0.02}_{-0.01}$	1.60 $^{+0.03}_{-0.02}$	878/894
P050523701402	60027.6	2.51 $^{+0.03}_{-0.04}$	0.65 $^{+0.04}_{-0.05}$	1.44 $^{+0.03}_{-0.03}$	26.89 $^{+12.30}_{-10.08}$	0.75 $^{+0.04}_{-0.02}$	2.66 $^{+0.02}_{-0.02}$	1.00 $^{+0.03}_{-0.03}$	904/894
P050523701701	60031.7	2.70 $^{+0.01}_{-0.01}$	1.00 $^{+0.00}_{-0.02}$	1.78 $^{+0.02}_{-0.02}$	14.46 $^{+3.19}_{-4.01}$	0.64 $^{+0.01}_{-0.01}$	3.09 $^{+0.01}_{-0.01}$	1.37 $^{+0.01}_{-0.01}$	891/894
P050523701703	60032.0	2.71 $^{+0.01}_{-0.02}$	1.00 $^{+0.00}_{-0.02}$	1.87 $^{+0.01}_{-0.01}$	12.30 $^{+3.00}_{-3.04}$	0.61 $^{+0.01}_{-0.01}$	3.23 $^{+0.01}_{-0.01}$	1.44 $^{+0.03}_{-0.02}$	890/894
P050523701802	60034.4	2.61 $^{+0.03}_{-0.03}$	1.00 $^{+0.00}_{-0.04}$	2.12 $^{+0.02}_{-0.03}$	7.99 $^{+2.30}_{-1.92}$	0.56 $^{+0.03}_{-0.03}$	3.35 $^{+0.03}_{-0.01}$	1.73 $^{+0.04}_{-0.03}$	885/894
P050523701901	60035.9	2.50 $^{+0.07}_{-0.05}$	0.38 $^{+0.04}_{-0.01}$	1.55 $^{+0.01}_{-0.02}$	21.03 $^{+6.21}_{-4.73}$	0.68 $^{+0.01}_{-0.01}$	2.96 $^{+0.01}_{-0.01}$	0.66 $^{+0.02}_{-0.02}$	868/894
P050523701903	60036.2	2.42 $^{+0.09}_{-0.05}$	0.31 $^{+0.04}_{-0.02}$	1.56 $^{+0.02}_{-0.02}$	21.10 $^{+7.60}_{-6.28}$	0.69 $^{+0.02}_{-0.01}$	2.87 $^{+0.01}_{-0.01}$	0.59 $^{+0.02}_{-0.02}$	856/894
P050523702001	60037.7	2.28 $^{+0.06}_{-0.04}$	0.23 $^{+0.02}_{-0.01}$	1.62 $^{+0.01}_{-0.02}$	20.79 $^{+5.99}_{-5.30}$	0.71 $^{+0.01}_{-0.01}$	3.03 $^{+0.01}_{-0.01}$	0.56 $^{+0.02}_{-0.02}$	911/894
P050523702101	60039.5	2.23 $^{+0.09}_{-0.05}$	0.18 $^{+0.02}_{-0.01}$	1.58 $^{+0.02}_{-0.01}$	20.80 $^{+5.28}_{-6.89}$	0.71 $^{+0.01}_{-0.02}$	2.73 $^{+0.01}_{-0.01}$	0.42 $^{+0.02}_{-0.02}$	946/894
P050523702201	60042.8	2.21 $^{+0.07}_{-0.05}$	0.16 $^{+0.02}_{-0.01}$	1.55 $^{+0.01}_{-0.01}$	20.54 $^{+5.37}_{-5.71}$	0.70 $^{+0.01}_{-0.01}$	2.61 $^{+0.01}_{-0.01}$	0.37 $^{+0.02}_{-0.02}$	952/894
P050523702301	60043.6	2.26 $^{+0.05}_{-0.04}$	0.20 $^{+0.01}_{-0.01}$	1.58 $^{+0.01}_{-0.01}$	20.12 $^{+5.26}_{-4.38}$	0.69 $^{+0.01}_{-0.01}$	2.76 $^{+0.01}_{-0.01}$	0.45 $^{+0.01}_{-0.01}$	920/894
P050523702402	60046.6	2.40 $^{+0.03}_{-0.04}$	0.38 $^{+0.02}_{-0.03}$	1.54 $^{+0.02}_{-0.02}$	15.38 $^{+4.21}_{-4.46}$	0.58 $^{+0.01}_{-0.01}$	2.63 $^{+0.01}_{-0.01}$	0.72 $^{+0.01}_{-0.01}$	909/894
P050523702501	60048.7	2.27 $^{+0.04}_{-0.04}$	0.23 $^{+0.02}_{-0.02}$	1.56 $^{+0.01}_{-0.01}$	17.27 $^{+4.04}_{-3.77}$	0.62 $^{+0.01}_{-0.01}$	2.85 $^{+0.01}_{-0.01}$	0.56 $^{+0.02}_{-0.02}$	1099/894
P050523702601	60050.5	2.01 $^{+0.06}_{-0.07}$	0.13 $^{+0.01}_{-0.02}$	1.58 $^{+0.02}_{-0.02}$	17.76 $^{+5.39}_{-4.69}$	0.64 $^{+0.01}_{-0.01}$	2.78 $^{+0.01}_{-0.01}$	0.49 $^{+0.02}_{-0.02}$	964/894
P050523702701	60052.7	2.02 $^{+0.08}_{-0.07}$	0.15 $^{+0.02}_{-0.02}$	1.61 $^{+0.01}_{-0.01}$	16.84 $^{+4.43}_{-3.67}$	0.63 $^{+0.01}_{-0.01}$	2.85 $^{+0.01}_{-0.01}$	0.54 $^{+0.02}_{-0.02}$	1027/894
P050523703301	60054.7	2.02 $^{+0.06}_{-0.04}$	0.14 $^{+0.01}_{-0.01}$	1.57 $^{+0.01}_{-0.01}$	18.28 $^{+4.46}_{-4.24}$	0.66 $^{+0.01}_{-0.01}$	2.51 $^{+0.01}_{-0.01}$	0.45 $^{+0.02}_{-0.02}$	963/894
P050523703401	60055.8	1.81 $^{+0.04}_{-0.09}$	0.06 $^{+0.01}_{-0.01}$	1.54 $^{+0.01}_{-0.01}$	17.13 $^{+4.40}_{-4.13}$	0.65 $^{+0.01}_{-0.01}$	2.16 $^{+0.01}_{-0.01}$	0.27 $^{+0.02}_{-0.02}$	905/894
P050523703602	60060.5	2.13 $^{+0.12}_{-0.02}$	0.15 $^{+0.03}_{-0.01}$	1.42 $^{+0.01}_{-0.01}$	25.68 $^{+7.45}_{-8.55}$	0.83 $^{+0.02}_{-0.03}$	1.80 $^{+0.01}_{-0.01}$	0.28 $^{+0.02}_{-0.02}$	910/894
P050523703901	60066.0	1.71 $^{+0.01}_{-0.16}$	0.08 $^{+0.01}_{-0.02}$	1.37 $^{+0.05}_{-0.01}$	22.96 $^{+7.53}_{-8.42}$	0.75 $^{+0.02}_{-0.03}$	1.45 $^{+0.07}_{-0.07}$	0.25 $^{+0.08}_{-0.08}$	895/894

- Narayan, R., & Yi, I. 1995, *ApJ*, 452, 710, doi: [10.1086/176343](https://doi.org/10.1086/176343)
- Peng, J.-Q., Zhang, S., Wang, P.-J., et al. 2023, *ApJ*, 955, 96, doi: [10.3847/1538-4357/acf461](https://doi.org/10.3847/1538-4357/acf461)
- Peng, J.-Q., Zhang, S., Shui, Q.-C., et al. 2024, *ApJL*, 965, L22, doi: [10.3847/2041-8213/ad3640](https://doi.org/10.3847/2041-8213/ad3640)
- Piran, T. 1978, *ApJ*, 221, 652, doi: [10.1086/156069](https://doi.org/10.1086/156069)
- Ratheesh, A., Dovčiak, M., Krawczynski, H., et al. 2024, *ApJ*, 964, 77, doi: [10.3847/1538-4357/ad226e](https://doi.org/10.3847/1538-4357/ad226e)
- Rawat, D., Garg, A., & Méndez, M. 2023, *MNRAS*, 525, 661, doi: [10.1093/mnras/stad2327](https://doi.org/10.1093/mnras/stad2327)
- Ren, X. Q., Wang, Y., Zhang, S. N., et al. 2022, *ApJ*, 932, 66, doi: [10.3847/1538-4357/ac6dd7](https://doi.org/10.3847/1538-4357/ac6dd7)
- Seifina, E., Titarchuk, L., & Shaposhnikov, N. 2014, *ApJ*, 789, 57, doi: [10.1088/0004-637X/789/1/57](https://doi.org/10.1088/0004-637X/789/1/57)
- Shakura, N. I., & Sunyaev, R. A. 1973, *A&A*, 24, 337
- Shapiro, S. L., Lightman, A. P., & Eardley, D. M. 1976, *ApJ*, 204, 187, doi: [10.1086/154162](https://doi.org/10.1086/154162)
- Shimura, T., & Takahara, F. 1995a, *ApJ*, 445, 780, doi: [10.1086/175740](https://doi.org/10.1086/175740)
- . 1995b, *ApJ*, 445, 780, doi: [10.1086/175740](https://doi.org/10.1086/175740)
- Tanaka, Y., & Shibazaki, N. 1996, *ARA&A*, 34, 607, doi: [10.1146/annurev.astro.34.1.607](https://doi.org/10.1146/annurev.astro.34.1.607)
- Tetarenko, B. E., Sivakoff, G. R., Heinke, C. O., & Gladstone, J. C. 2016a, *VizieR Online Data Catalog*, J/ApJS/222/15
- . 2016b, *ApJS*, 222, 15, doi: [10.3847/0067-0049/222/2/15](https://doi.org/10.3847/0067-0049/222/2/15)
- Thorne, K. S., & Price, R. H. 1975, *ApJL*, 195, L101, doi: [10.1086/181720](https://doi.org/10.1086/181720)
- Tomsick, J. A., Lapshov, I., & Kaaret, P. 1998, *ApJ*, 494, 747, doi: [10.1086/305240](https://doi.org/10.1086/305240)

- Tomsick, J. A., Yamaoka, K., Corbel, S., et al. 2014, *ApJ*, 791, 70, doi: [10.1088/0004-637X/791/1/70](https://doi.org/10.1088/0004-637X/791/1/70)
- Verner, D. A., Ferland, G. J., Korista, K. T., & Yakovlev, D. G. 1996, *ApJ*, 465, 487, doi: [10.1086/177435](https://doi.org/10.1086/177435)
- Watarai, K.-y., Fukue, J., Takeuchi, M., & Mineshige, S. 2000a, *PASJ*, 52, 133, doi: [10.1093/pasj/52.1.133](https://doi.org/10.1093/pasj/52.1.133)
- . 2000b, *PASJ*, 52, 133, doi: [10.1093/pasj/52.1.133](https://doi.org/10.1093/pasj/52.1.133)
- Wilms, J., Allen, A., & McCray, R. 2000, *ApJ*, 542, 914, doi: [10.1086/317016](https://doi.org/10.1086/317016)
- Zhang, S., Lu, F. J., Zhang, S. N., & Li, T. P. 2014, in *Society of Photo-Optical Instrumentation Engineers (SPIE) Conference Series*, Vol. 9144, *Space Telescopes and Instrumentation 2014: Ultraviolet to Gamma Ray*, ed. T. Takahashi, J.-W. A. den Herder, & M. Bautz, 914421, doi: [10.1117/12.2054144](https://doi.org/10.1117/12.2054144)
- Zhang, S., Zhang, S. N., Lu, F. J., et al. 2018, in *Society of Photo-Optical Instrumentation Engineers (SPIE) Conference Series*, Vol. 10699, *Space Telescopes and Instrumentation 2018: Ultraviolet to Gamma Ray*, ed. J.-W. A. den Herder, S. Nikzad, & K. Nakazawa, 106991U, doi: [10.1117/12.2311835](https://doi.org/10.1117/12.2311835)
- Zhang, S.-N., Li, T., Lu, F., et al. 2020, *Science China Physics, Mechanics, and Astronomy*, 63, 249502, doi: [10.1007/s11433-019-1432-6](https://doi.org/10.1007/s11433-019-1432-6)